ACS OMEGA

http://pubs.acs.org/journal/acsodf

Article

In Situ Growth of MnO_2 Nanosheets on a Graphite Flake as an Effective Binder-Free Electrode for High-Performance Supercapacitors

Yuanhang Gu,[‖] Dong Xu,[‖] Shaoyun Chen, Feng You, Chenglong Hu,* Huabo Huang,* and Jian Chen

Cite This: *ACS Omega* 2022, 7, 48320−48331

Read Online

ACCESS | Metrics & More | Article Recommendations

ABSTRACT: In this work, manganese dioxide (MnO_2) nanosheets in situ loaded on a high-purity graphite flake (GF) were prepared by one-step hydrothermal deposition. It was found that the specific capacitance value of a single MnO_2/GF electrode was 882 F/g at a current density of 1.0 A/g in a KOH electrolyte, and the specific capacitance retention of the MnO_2/GF electrode can reach about 90.1% after 5000 charge−discharge cycles at a current density of 10 A/g. Furthermore, a MnO_2/GF‖MnO_2/GF symmetric supercapacitor device was fabricated with two pieces of MnO_2/GF electrodes and ordinary filter paper with a 1 M KOH/PVA gel electrolyte as a separator. The single symmetric device displayed a high energy density of 64.2 Wh/kg at a power density of 400 W/kg within an applied voltage of 1.6 V, and this value was superior to those of previously reported MnO_2-based systems. A tandem device consisting of a five-series tandem device (the applied voltage of a single device was 0.7 V) and a three-series tandem device (the applied voltage of a single device was 1.6 V) was prepared to drive a red light-emitting diode (LED). These findings open up application prospects for MnO_2-based composite electrode materials for high-performance supercapacitors.

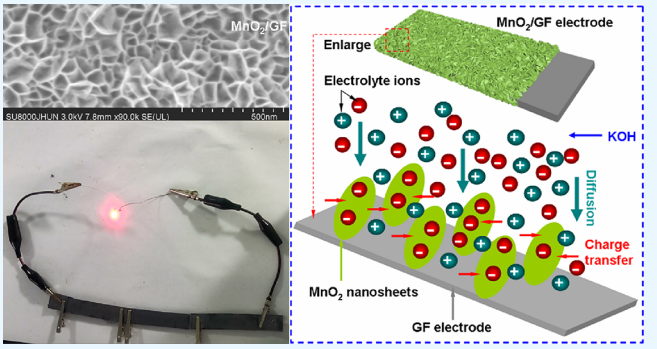

1. INTRODUCTION

In recent years, with the rapid development of portable, mobile, and wearable electronic devices, supercapacitors have gradually entered people's daily lives.[1,2] It is well known that electrode materials, electrolytes, and separators influence the energy density and power density of supercapacitors.[3,4] In particular, the type of electrode material directly determines the structure and electrochemical performance of supercapacitors.[5,6] Therefore, exploring suitable electrode materials has become the main research direction for improving the energy storage density of supercapacitors. The electrode materials of supercapacitors can be mainly divided into three categories: carbon materials,[7,8] metal oxides,[5,9] and conductive polymers.[10−12] Since the reversible Faradaic pseudocapacitance of transition metal oxides at the electrode/solution interface is much larger than the electric double-layer capacitance produced by carbon materials, transition metal oxides have attracted the attention of researchers. For example, $NiCo_2O_4$,[13] NiO,[14] Co_3O_4,[15] $Ni_xCo_{3-x}O_4$,[16] MoO_3,[17] MnO_2,[18−20] Ti_3C_2TX,[21] Fe_2O_3,[22] V_2O_5,[23] RuO_2,[24] WO_3,[25] and bimetallic oxides (MN_2O_4, where M or N is Ni, Co, Zn, Mn, Fe, Cu, etc.)[26] have been usually used as electrode materials for supercapacitors.

Compared with other metal materials, MnO_2 has the characteristics of wide potential window (about 1 V), wide source of raw materials, and environmental friendliness.[27−30] Moreover, the large specific surface area and high pseudocapacitance of nanoscale MnO_2 can exhibit good applied advantages when it is used as an electrode material for supercapacitors.[31] For instance, Yu et al. reported that printed polyacrylonitrile (PAN) was used as a scaffold to deposit highly ordered MnO_2 nanopillars for supercapacitor materials, and the specific capacitance (SC) was 603 F/g at a scan rate of 5 mV/s.[32] Zhang et al. showed that the electrochemical performance of pure MnO_2 could be improved using the electrodeposition method by controlling the applied voltages, and the SC value could reach as high as 469 F/g at a current density of 1 A/g when the applied voltage was controlled at 0.6 V.[33] Wu et al. reported that 3D plate-like MnO_2 materials could be obtained using a novel nickel foam supporting

Received: October 9, 2022
Accepted: November 30, 2022
Published: December 13, 2022

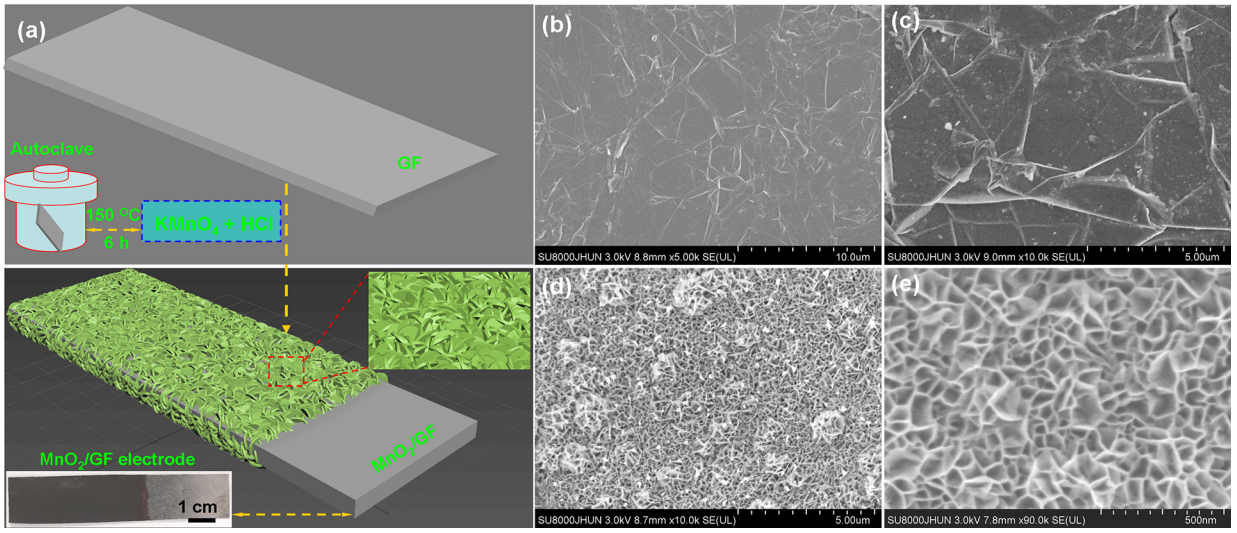

Figure 1. (a) Schematic diagram of the prepared MnO_2/GF. (b, c) SEM images of the GF surface at low and high magnifications, respectively. (d, e) SEM images of the MnO_2/GF surface at low and high magnifications, respectively.

substrate, and the 3D MnO_2 electrode exhibited a high SC value of 680.6 F/g at a scan rate of 1 mV/s.[34] However, the low conductivity (10^{-5}–10^{-6} S/cm) of MnO_2 makes it difficult for it to show its full electrochemical performance when it is used alone as an electrode material for supercapacitors.[35] At the same time, there will be also problems such as faster decay of SC and poor long-term cycle stability. Currently, one of the best ways to solve this problem is to prepare composite electrode materials based on MnO_2 and improve the comprehensive performance of supercapacitors utilizing the synergistic effect of each component. MnO_2 combined with carbon nanotubes,[27] graphene,[36] and other carbon materials[37] with good conductivity is an effective way to solve this problem. Jia et al. showed that carbon nanotubes in situ grew onto vertically aligned MnO_2 nanosheets with nanopores to form an electrode for supercapacitors, and the SC value was 1229 F/g at a current density of 1 A/g.[38] Saraf et al. prepared a nitrogen-doped reduced graphene oxide–MnO_2 nanocomposite by the one-pot hydrothermal method to apply in supercapacitors, and the SC value could reach 648 F/g at 1.5 A/g.[39] Li et al. reported that MnO_2 nanosheets could be easily grown on the inner surface of macroporous carbon to increase the utilization rate of the active material, and the maximum SC value was 1332 F/g at a 150 μg/cm^2 loading of active material.[40]

Based on our previous work,[41−46] in this work, we used a simple hydrothermal method for in situ growth of MnO_2 nanosheets on high-purity graphite flakes (GFs) with good electrical conductivity, and the electrochemical performances of a single MnO_2/GF electrode and a symmetrical MnO_2/GF||MnO_2/GF device were also systematically studied with a three-electrode and a two-electrode system, respectively. It was found that the SC value of a single MnO_2/GF electrode was 882 F/g in a 1 M KOH electrolyte, and the energy density (E) was 64.2 Wh/kg at a power density (P) of 400 W/kg. The advantages of the as-prepared composites as electrode materials are as follows: (i) The as-prepared electrode does not need to have the substrate coated with acetylene black and binder to prepare the working electrode, and the MnO_2 nanosheets grow on the surface of the conductive support substrate, which can greatly reduce the internal resistance of the electrode material to improve the electrochemical performance of the active electrode. (ii) Due to the fact that the as-prepared electrode system has a self-supporting electrode material (GF), the preparation process is simplified and the proportion of pseudocapacitive materials is increased, and thereby, the interaction between the electrode and substrate is enhanced, which is beneficial to the transfer of electrons in electrochemical reactions. (iii) The preparation method is simple, which can be easily carried out in general laboratories.

2. EXPERIMENTAL SECTION

2.1. Synthesis of MnO_2 Nanosheets Growing onto a GF (I.e., MnO_2/GF). The GF was obtained from North China Science and Technology Metal Material Co. Ltd. (China). The potassium permanganate ($KMnO_4$), poly(vinyl alcohol) (PVA), hydrochloric acid (HCl), and ethanol used were analytical grade reagents that were purchased from Sinopharm Chemical Reagent Co., Ltd. (Shanghai, China).

The GF was firstly cut into uniform strips with a size of 2 × 5 cm^2 to form a supporting electrode, and then sonicated in acetone, ethanol, and deionized water for 10 min, respectively, and dried at 60 °C for 2 h. 0.4266 g of $KMnO_4$ and 0.2 mL of HCl (12 M) were added into 30 mL of deionized water to form a 0.09 M $KMnO_4$ solution by magnetic stirring. The as-prepared $KMnO_4$ solution was transferred into a 50 mL autoclave, and the GF was placed leaning against the inner wall of the autoclave. The autoclave was hydrothermally reacted in an oven with a temperature of 150 °C for 6 h. It is noted that MnO_2 nanosheets could well grow on both sides of the GF and one side with nanosheets was kept for studying; the other side was removed with lens cleaning paper. The mass loading of MnO_2 on the GF is about 2 × 10^{-3} g.

2.2. Design of an All-Solid-State Symmetrical MnO_2/GF||MnO_2/GF Supercapacitor. 3.0 g of PVA powder and 1.68 g of KOH were added into 30 mL of distilled water to prepare a 1 M KOH/PVA hydrogel electrolyte. The MnO_2/GF electrodes and filter paper (as separator) were immersed into the KOH/PVA solution for 24 h, and then two sheets of MnO_2/GF electrodes and a filter paper were stacked together to form an all-solid-state symmetric MnO_2/GF||MnO_2/GF

https://doi.org/10.1021/acsomega.2c06506
ACS Omega 2022, 7, 48320−48331

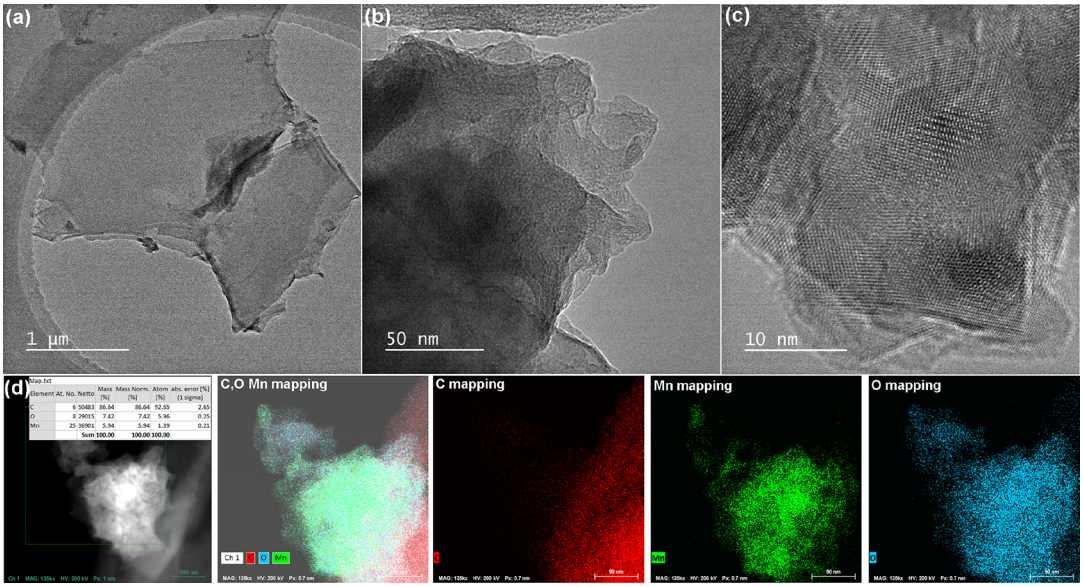

Figure 2. (a–c) TEM images of the MnO_2/GF surface at low and high magnifications. (d) Chemical element mapping of individual elements of the as-prepared MnO_2/GF.

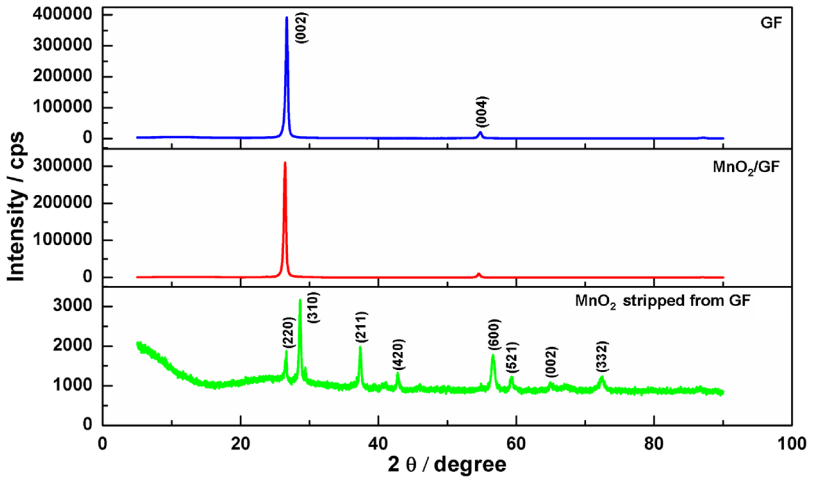

Figure 3. XRD patterns of the GF, MnO_2/GF, and MnO_2 stripped from the GF.

supercapacitor device. The electrochemical performance of device was measured after drying at room temperature.

2.3. Characterization. Cyclic voltammetry (CV), galvanostatic charge–discharge (GCD), and electrochemical impedance spectroscopy (EIS) of a single MnO_2/GF electrode and symmetrical MnO_2/GF||MnO_2/GF were carried out with a three-electrode (saturated calomel electrode as the reference electrode, platinum plate electrode as the counter electrode, and MnO_2/GF as the working electrode) and a two-electrode system using an electrochemical workstation (CHI 660E, Shanghai Chenhua Inc., China). Field-emission scanning electron microscopy (FE-SEM, SU8000, Hitachi), X-ray photoelectron spectroscopy (XPS, Axis Supra$^+$, Hitachi), Raman spectroscopy (532 nm inVia laser, Renishaw), and X-ray diffraction (XRD, Panalytical X' Pert powder diffractometer) were used to study the morphology and structure of the as-prepared electrode.

3. RESULTS AND DISCUSSION

In situ growth of MnO_2 nanosheets on a GF originates from the redox reaction of $KMnO_4$ and carbon under hydrothermal conditions, and the GF is used as a reducing agent and electrode scaffolds, as shown in Figure 1a. The reaction formula is as follows:[47]

$$4KMnO_4 + 3C + 4HCl = 4MnO_2 + 3CO_2 + 4KCl + 2H_2O \quad (1)$$

The morphologies of the GF and MnO_2/GF can be characterized by SEM, as shown in Figure 1b–e. It can be seen that the surface of the GF is very flat and clean, and no other impurities are attached to the surface, as shown in Figure 1b. From Figure 1c, it can be also seen that the GF is composed of a lot of thin graphite sheets, and this relaxed structure is conducive to the in situ growth of metal oxide. Figure 1d shows that MnO_2 nanosheets can be uniformly and densely decorated on the surface of the GF. Meanwhile, a few MnO_2 clusters are formed on the surface of the GF; these

https://doi.org/10.1021/acsomega.2c06506
ACS Omega 2022, 7, 48320–48331

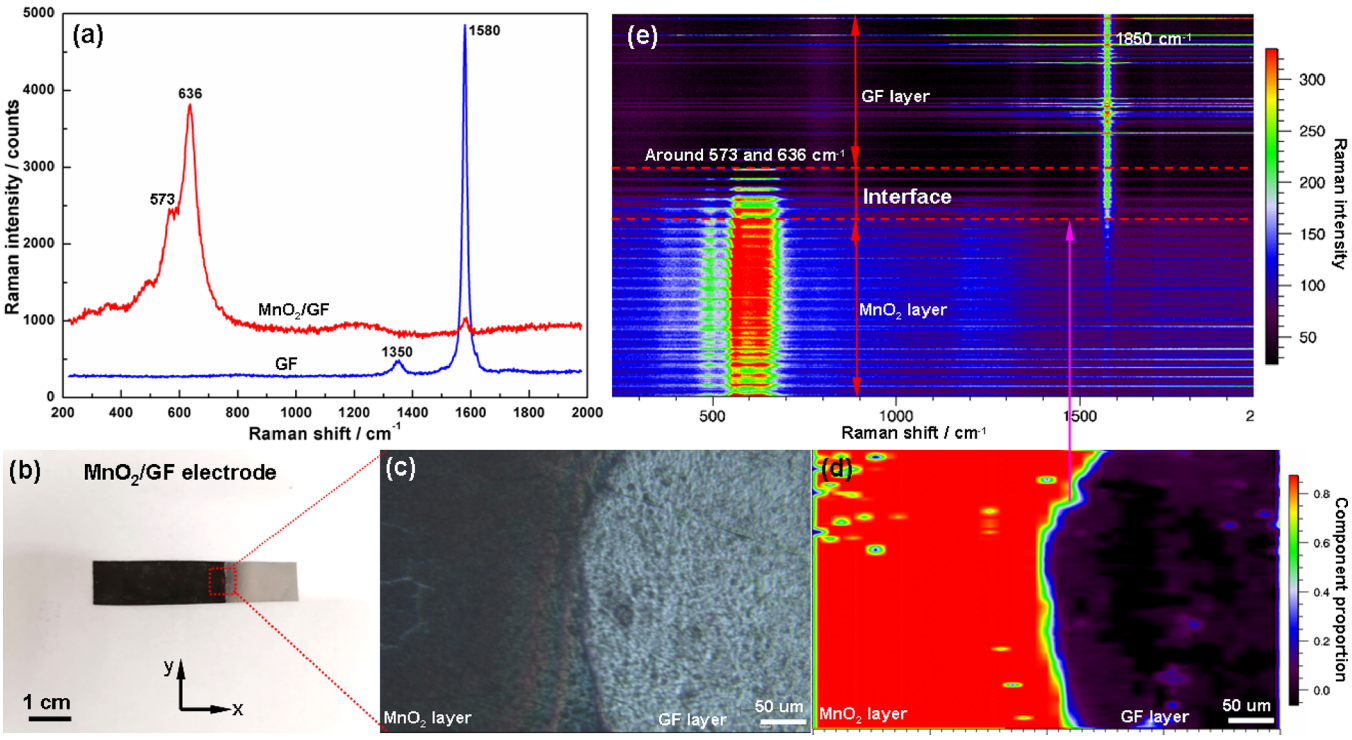

Figure 4. (a) Raman spectra of the GF and MnO_2/GF. (b, c) Optical images of the MnO_2/GF electrode. (d) Raman mapping of the chemical component of the selected region in the MnO_2/GF electrode. (e) 2D overlay Raman mapping transformed from panel (d).

originate from the decomposition of $KMnO_4$ during the reaction. Figure 1e shows that the MnO_2 nanosheets with a thickness of about 10 nm are interconnected with each other to form an ordered nanonetwork structure, and the advantages of this structure are as follows: (i) The small size of MnO_2 nanosheets favors enlarging the contact interface between the active material and the electrolyte to contribute a big pseudocapacitance. (ii) The open space of the MnO_2 nanonetwork structure can effectively accelerate ion diffusion in the electrolyte. The TEM image of MnO_2/GF shows that MnO_2 grows on graphite sheets in interlaced sheets (Figure 2a,b), and a lot of clear lattice fringes can be observed in the high-resolution image of MnO_2 (Figure 2c), indicating that the MnO_2 nanosheets prepared onto the surface of the GF has high crystallinity. The chemical element mapping of individual elements of the as-prepared MnO_2/GF can be found in Figure 2d. The C element comes from the GF; the Mn and O elements originate from MnO_2.

The XRD patterns of the GF and MnO_2/GF can be found in Figure 3. The peaks of (002) and (004) are the two strongest peaks in the XRD pattern of natural graphite, representing the direction perpendicular to the hexagonal graphite plane (*c* axis).[48,49] The intensities of the (002) and (004) diffraction peaks reach about 400,000 and 10,000 cps, respectively, indicating that the GF has good crystallization (blue line). However, the intensities of the (002) and (004) diffraction peaks decrease significantly compared with those of pure GF when MnO_2 nanosheets grow on the surface of the GF, which indicates that MnO_2 nanosheets can well adhere to the surface of a GF. Moreover, due to the thin thickness of MnO_2 nanosheets grown on the GF and the good crystallinity of the GF, it is difficult to show the diffraction peaks of MnO_2 on the XRD curve (red line). In order to detect the diffraction peaks of MnO_2 nanosheets, we carefully removed the MnO_2 nanosheets from the surface of the GF by the method of blade peeling, and the result can be found in Figure 3 (green line). MnO_2 has eight distinct characteristic peaks located at 2θ = 26.6, 28.6, 37.3, 43.0, 56.7, 59.3, 65.0, and 72.5°, corresponding to (220), (311), (211), (420), (600), (521), (002), and (332) of MnO_2 crystal planes (JCPDS No. 44-0114).[50] The result indicates that MnO_2 nanosheets can well grow on the surface of a GF.

The Raman spectra of the GF and MnO_2/GF can be found in Figure 4a. For the GF, there are two distinct scattering peaks appearing at 1580 and 1350 cm^{-1}, which are assigned to the G band (the E^2/g mode in the basal plane of graphite) and D band (the disorder characteristic due to the finite particle size effect and lattice distortion).[48] Moreover, the high intensity of G bands and the weak intensity of D bands indicate that the GF has a good degree of crystallinity, corresponding with the result of XRD. In the Raman spectrum of the as-prepared MnO_2/GF electrode, the Mn−O lattice vibration can be found at the peak of 573 cm^{-1}, while the peak at 637 cm^{-1} is assigned to the Mn−O lattice vibration in Mn_3O_4 because the localized sample is slightly heated by laser irradiation.[50] In addition, the weak intensity of G bands can be also found in the Raman spectrum of MnO_2/GF, revealing that MnO_2 can well grow on the surface of a GF, as shown in Figure 4b,c. To further confirm the growth of MnO_2 on the GF surface, Raman mapping of the chemical component of a selected region in the MnO_2/GF electrode was carried out at an excited wavelength of 532 nm, and the result is shown in Figure 4d. Obviously, the red region is mostly a MnO_2 layer, and the deep purple region is the pure GF layer, which is consistent with the result of optical images in Figure 4b,c. The 2D overlay Raman mapping transformed from Figure 4d is shown in Figure 4e. It can be found that only one scattering peak at 1580 cm^{-1} is observed in the GF layer, and the 2D overlay Raman signals of MnO_2

https://doi.org/10.1021/acsomega.2c06506
ACS Omega 2022, 7, 48320−48331

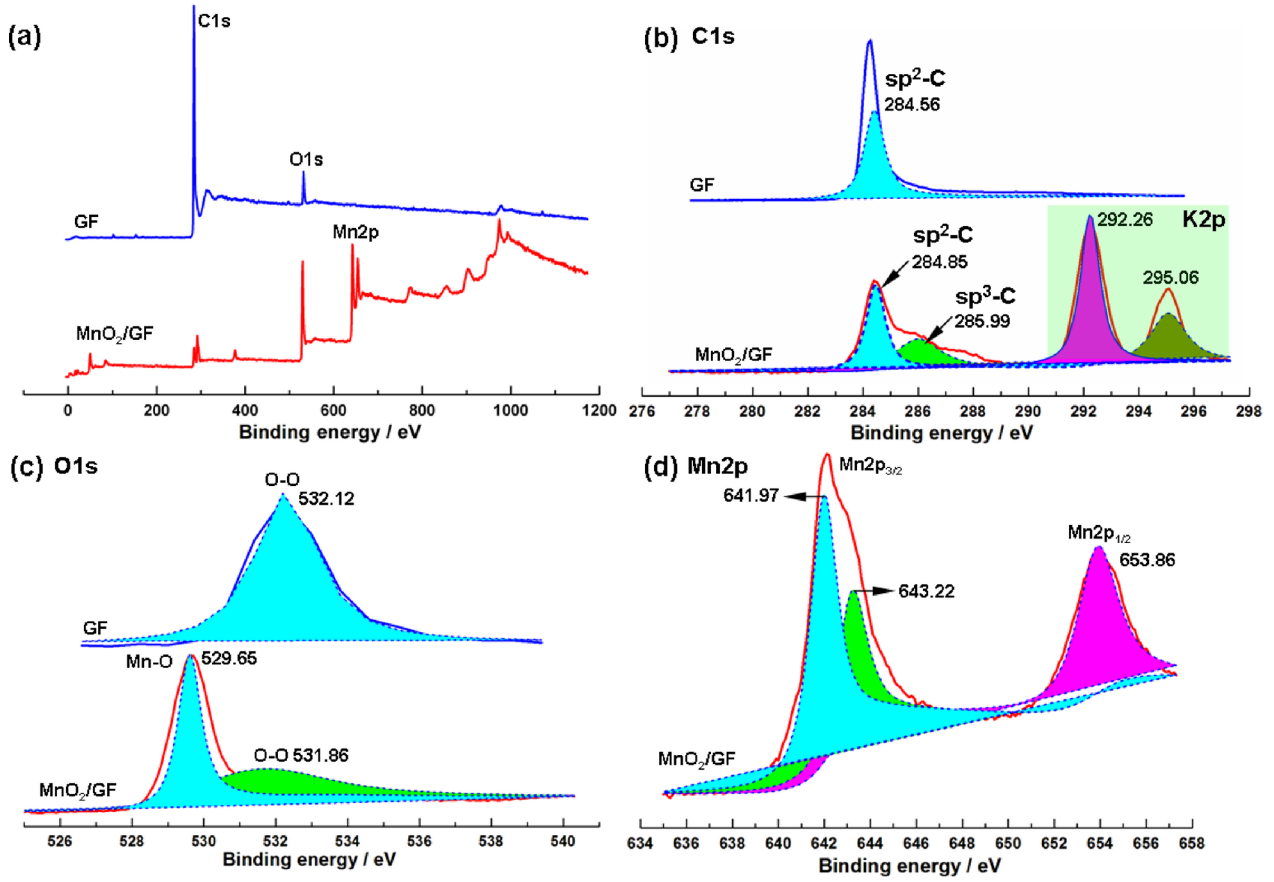

Figure 5. (a) XPS survey spectra of the GF and MnO_2/GF. (b) C 1s core-level spectra of the GF and MnO_2/GF. (c) O 1s core-level spectra of the GF and MnO_2/GF. (d) Mn 2p core-level spectrum of MnO_2/GF.

are at around 573 and 637 cm^{-1}. Apparently, MnO_2 can be effectively and directly grown on the GF surface to prepare binder-free self-supporting electrodes.

To determine accurately the chemical structure of the product, XPS analysis was performed for the GF and MnO_2/GF, as shown in Figure 5a. For the GF, only the elements C and O are found in the survey spectrum, and C 1s (284.56 eV) and O 1s (532.12) are assigned to the sp^2-C and O−O groups, as shown in Figure 5b,c. For MnO_2/GF, it can be seen that the elements C, O, Mn, and K are present in the survey spectrum. C 1s (284.85 eV) and C 1s (286.99) are assigned to sp^2-C and sp^3-C,[51] revealing a chemical reaction between C and $KMnO_4$, as shown in eq 1. The high-resolution spectrum of K 2p has two main peaks with binding energies of 292.26 and 295.06 eV, corresponding to K $2p_{3/2}$ and K $2p_{1/2}$ spin−orbit splitting photoelectrons, respectively, which originates from the residual K element. The high-resolution spectrum of O 1s has two main peaks with binding energies of 529.65 and 531.86 eV, corresponding to Mn−O and O−O groups. Figure 5d shows the high-resolution spectrum of Mn 2p in MnO_2/GF. It is found that the separation value between Mn $2p_{1/2}$ (653.86 eV) and Mn $2p_{3/2}$ (641.97 eV) is 11.89 eV, indicating the chemical valence state of the as-synthesized manganese oxide is +4 (MnO_2).[52,53]

The electrochemical properties of single GF and MnO_2/GF electrodes were tested by the three-electrode framework. The CV curves of the samples in a 1 M KOH electrolyte at a scan rate of 10 mV/s are shown in Figure 6a. It can be seen that the area of the CV curve for the MnO_2/GF electrode is larger than that of the GF electrode. The GCD curves of the samples in a 1 mol/L KOH electrolyte at a current of 1 A/g are shown in Figure 6b. It is found that the charge−discharge time of the MnO_2/GF electrode is much longer than that of the MnO_2 electrode. The results indicate that the recombination of MnO_2 and the GF can effectively improve the SC. In order to determine the most suitable working voltage when the MnO_2/GF electrode is used as the supercapacitor, the CV curves of the MnO_2/GF electrode at different operating voltages ranging from 0.6 to 1.0 V are recorded in Figure 6c. As can be seen from Figure 6c, the shape of the CV curve is almost exactly the same when the working voltage exceeds 0.7 V, showing that the MnO_2/GF electrode can stably work at 1.0 V when the as-prepared electrode is subjected to CV testing using the three-electrode framework. Figure 6d shows the GCD curves at different operating voltages from 0.5 to 0.9 V. Obviously, the GCD curves show a symmetrical triangle at voltages from 0.5 to 0.8 V, which comes from the pseudocapacitance. However, the GCD curve appears abnormal when the operating voltage window is expanded to 0.9 V, showing that the MnO_2/GF electrode can stably work below 0.8 V when the as-prepared electrode is subjected to GCD testing using the three-electrode framework. Therefore, in combination with the CV results, the voltage window is set between −0.3 and 0.4 V (0.7 V) to ensure successful CV and GCD testing.

Figure 7a shows the CV curves of the MnO_2/GF electrode at scan rates from 10 to 100 mV/s in a potential window of 0.7 V. It is observed that the CV curve presents a quasi-rectangular shape and a pair of redox peaks appearing at a low scan rate,

https://doi.org/10.1021/acsomega.2c06506
ACS Omega 2022, 7, 48320−48331

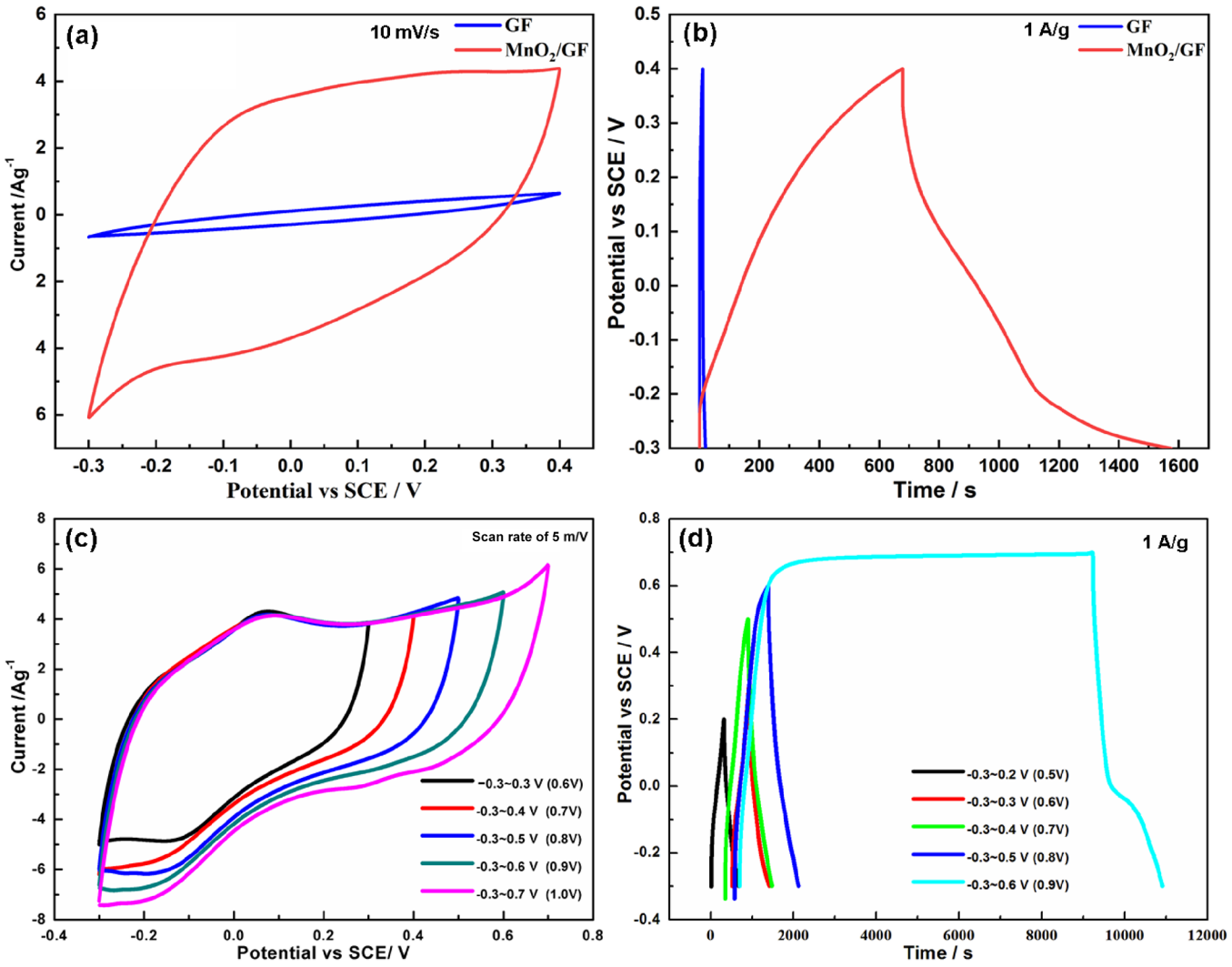

Figure 6. (a) CV curves of the GF and MnO_2/GF electrodes. (b) GCD curves of the GF and MnO_2/GF electrodes. (c) CV curves of the MnO_2/GF electrode at different operating voltages ranging from 0.6 to 1.0 V. (d) GCD curves of the MnO_2/GF electrode at different operating voltages ranging from 0.5 to 0.9 V.

indicating that the MnO_2/GF composite electrode exhibits both pseudocapacitive and electric double-layer properties. Moreover, all of the CV curves are rectangle-like and show good symmetry at different scan rates, which indicates that the internal structure of the MnO_2/GF electrode material has less resistance to charge transfer and electrolyte ion diffusion, and the as-prepared MnO_2/GF electrode can well work at large currents with good reversibility, as shown in Figure 7b. The GCD curves of the MnO_2/GF electrode at different current densities are relatively symmetrical triangles, showing an ideal capacitance behavior, as shown in Figure 7c. In addition, the capacity of the MnO_2/GF electrode decreases with an increase of current density; this is caused by the fact that the chemical response speed is slow due to the internal resistance of the MnO_2/GF electrode with increasing current density, which affects the expression of capacity. This is also a common problem in current supercapacitor research, and the other important indicator is whether an electrode can maintain a good SC under high currents for evaluating the electrochemical performance of supercapacitors. The SC of the MnO_2/GF electrode can be calculated as follows:[54]

$$SC = \frac{\Delta t \times I}{\Delta V \times m} \quad (2)$$

where Δt, I, m, and ΔV are the discharge time (s), the discharge current (A), the mass of one electrode (g), and the potential window (V), respectively. The calculated results can be found in Figure 7d. The maximum SC of the MnO_2/GF electrode is 882 F/g at a current density of 1 A/g, and the MnO_2/GF electrode still has an SC of 435 F/g even when the current density decreases to 5 A/g, revealing the good rate capability of the MnO_2/GF electrode. This is attributed to two main reasons: (i) The combination of the GF and MnO_2 endows the as-prepared electrode with excellent electrical conductivity and good interface contact between the active materials and electrolyte. (ii) The internal orderly network structure of MnO_2 nanosheets not only facilitates charge migration but also shortens the charge transport to accelerate charge transport at high current densities. (iii) The GF as a self-supporting electrode has good electrical conductivity that can quickly transfer electrons during the reaction.

Long-term cycling stability is another important parameter for evaluating the electrochemical performance of supercapacitors. The SC retention of the MnO_2/GF electrode can

https://doi.org/10.1021/acsomega.2c06506
ACS Omega 2022, 7, 48320−48331

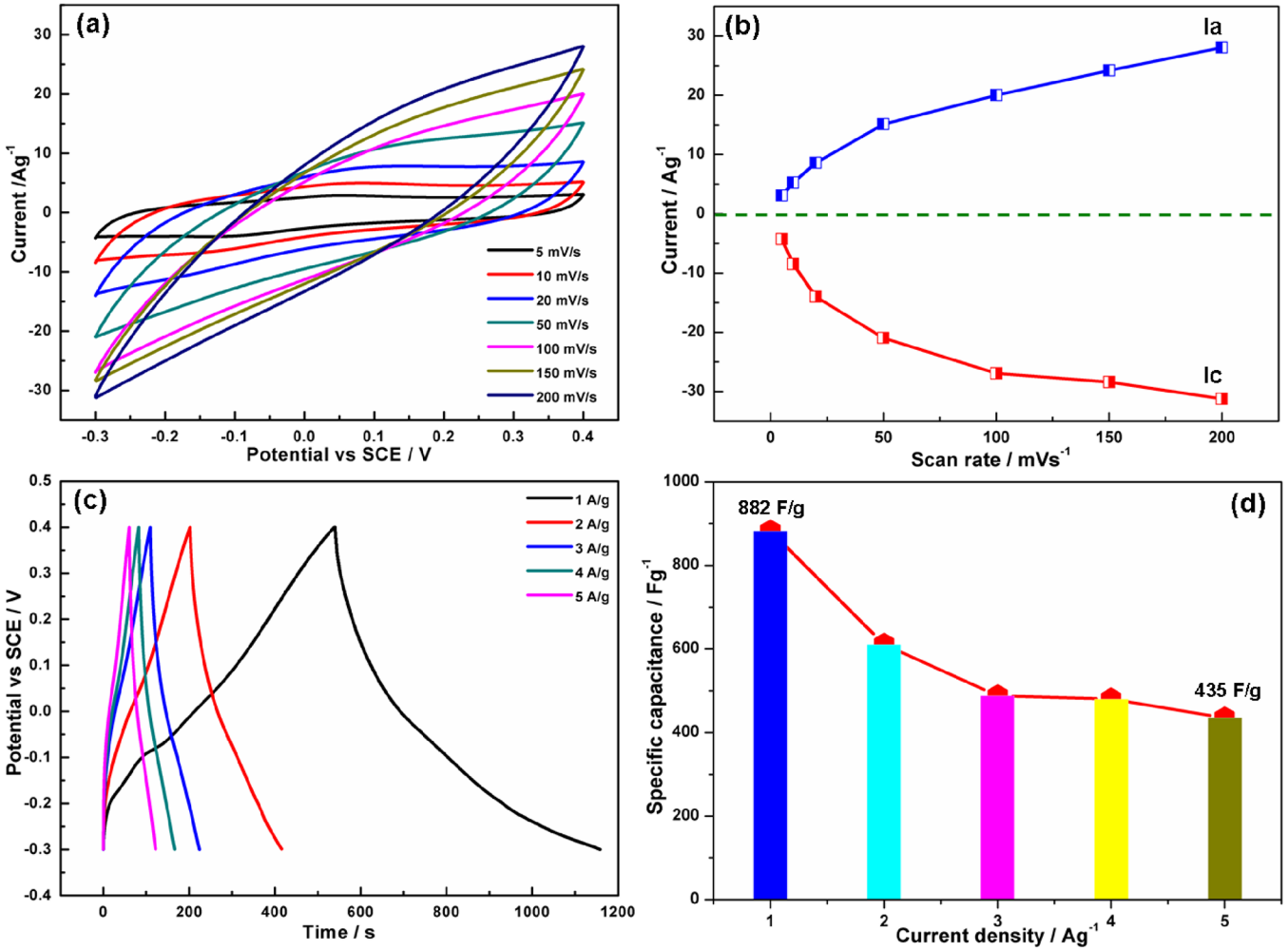

Figure 7. (a) CV curves of the MnO_2/GF electrode at scan rates from 10 to 100 mV/s in a potential window of 0.7 V. (b) Relationship of the maximum currents of CV curves with different scan rates. (c) GCD curves of the MnO_2/GF electrode at current densities from 1 to 5 A/g in a potential window of 0.7 V. (d) Relationship of the specific capacitance of the MnO_2/GF electrode with different current densities.

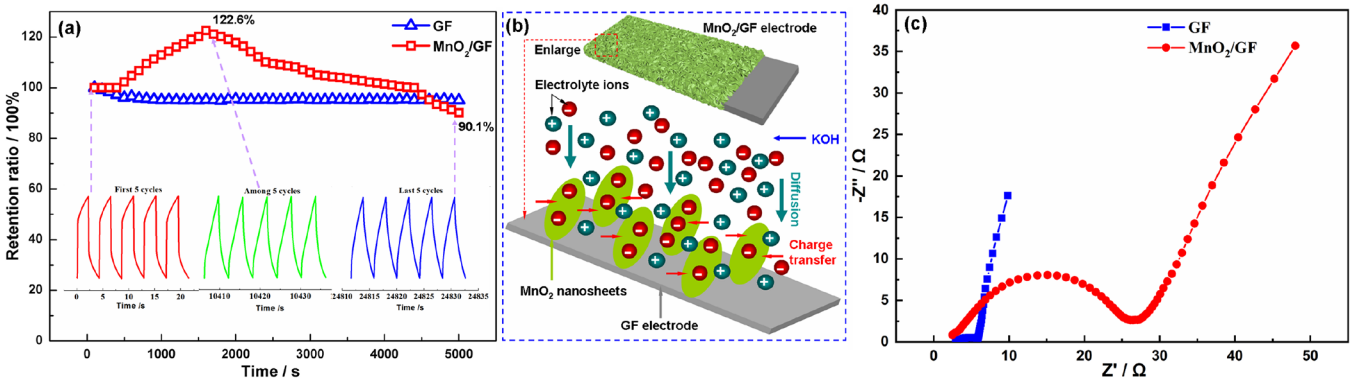

Figure 8. (a) Long-term cycling stability of the GF and MnO_2/GF electrodes. (b) Schematic of the optimized ion diffusion path in MnO_2 nanosheets. (c) Nyquist curves of the GF and MnO_2/GF electrodes.

reach about 122.6% after 1600 charge−discharge cycles with a current density of 10 A/g, as shown in Figure 8a. The enhanced SC retention is attributed to the following possible reasons: In the early stage of the electrochemical reaction, the ions only stay on the surface of the MnO_2 nanosheets to participate in the chemical reaction due to the poor conductivity of the MnO_2 nanosheets. Therefore, only a small amount of the active material participates in the electrochemical reaction to generate a relatively low SC. With the continuous progress of the electrochemical reaction, more ions penetrate into the interior of the MnO_2 nanosheets to participate in the reaction, greatly increasing the SC of the electrode, as shown in Figure 8b. However, the SC retention of the MnO_2/GF electrode decreases to 90.1% after 5000 cycles at a current density of 10 A/g. This is attributed to MnO_2 being consumed with the continuous reaction after the

https://doi.org/10.1021/acsomega.2c06506
ACS Omega 2022, 7, 48320−48331

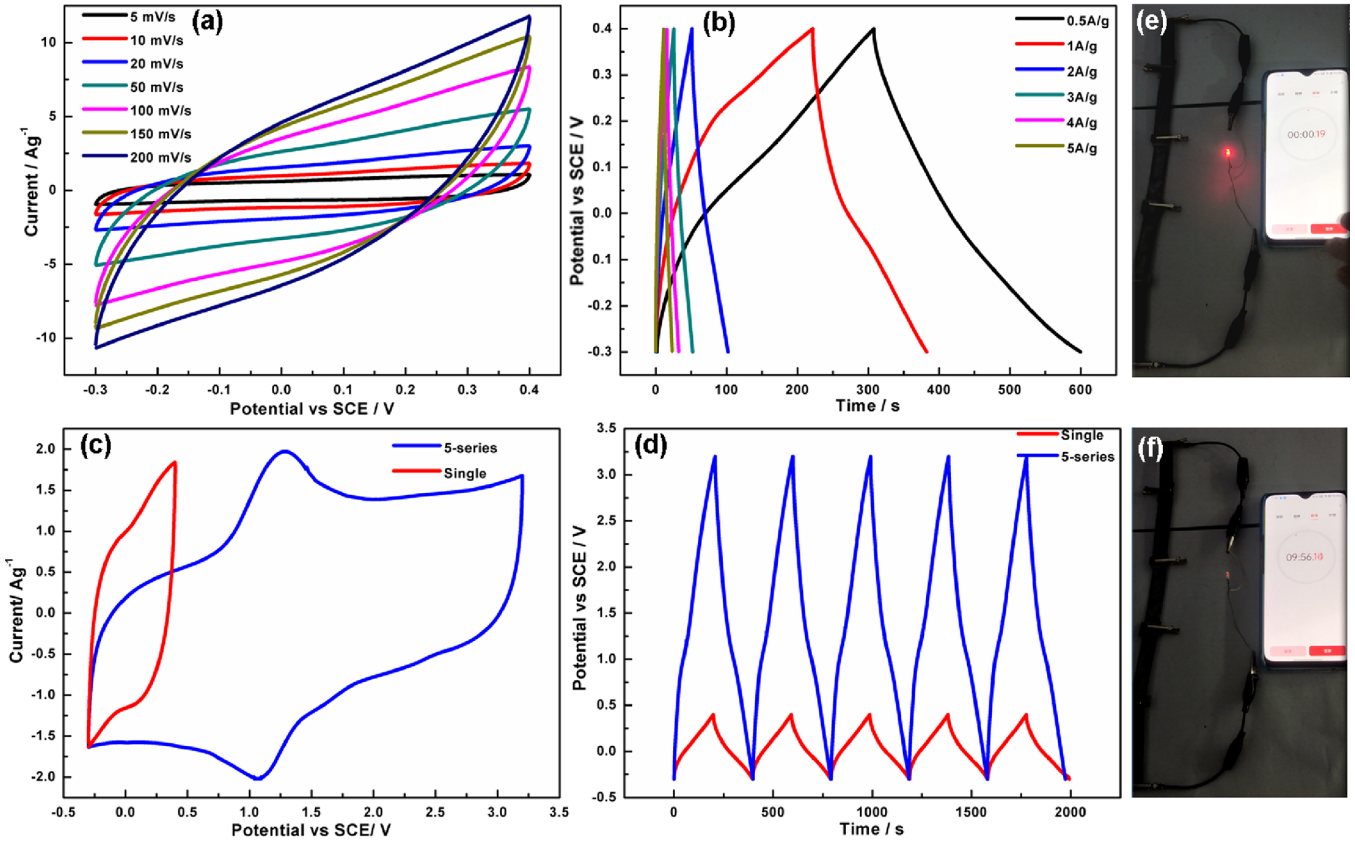

Figure 9. (a) CV curves of the single MnO_2/GF||MnO_2/GF symmetric device at different scan rates ranging from 5 to 200 mV/s (the applied voltage of a single device is 0.7 V). (b) GCD curves of the single MnO_2/GF||MnO_2/GF symmetric device at different current densities ranging from 0.5 to 5 A/g (the applied voltage of a single device is 0.7 V). (c) CV curves of the single symmetric device and five-series system at a scan rate of 5 mV/s. (d) GCD curves of the single symmetric device and five-series system at a current density of 1 A/g. (e, f) Photographs of the red LED driven by the five-series tandem device before and after about 10 min, respectively.

electrochemical reaction reaches saturation, decreasing the SC. The GCD curves of the MnO_2/GF electrode before and after 5000 charge−discharge cycles can be found in the inset of Figure 8a.

To further study the electrochemical properties of the MnO_2/GF electrode, EIS tests of the GF and MnO_2/GF electrodes were carried out in the frequency range of 0.01−100,000 Hz, and the obtained Nyquist curves are shown in Figure 8c. It can be seen that the MnO_2/GF electrode presents an incomplete semicircle in the high-frequency region, and the diameter of the semicircle represents the charge-transfer resistance at the interface between the active material and electrolyte.[55] The semicircle of the GF electrode is smaller than that of the MnO_2/GF electrode because the conductivity of pure GF is better than that of MnO_2/GF. In the low-frequency region, the Nyquist curves of the GF and MnO_2/GF electrodes are close to a straight vertical abscissa, and the slopes of the two curves are significantly close in the low-frequency region, indicating high diffusion and penetration efficiency of the electrolyte in the MnO_2/GF electrode, obtaining a good capacitance.

To further verify the practical application of MnO_2/GF electrodes, a MnO_2/GF||MnO_2/GF symmetric supercapacitor device was fabricated and its electrochemical behaviors were tested by two-electrode system, as shown in Figure 9. Apparently, the CV curves of the single symmetric device exhibit a quasi-rectangular shape at different scan rates, indicating that the as-prepared single symmetric device has an excellent double-layer capacitance behavior in operating potentials ranging from −0.3 to 0.4 V (Figure 9a). The GCD curves of the single symmetric device are nearly triangular at different current densities, indicating the good electrochemical reversibility and Coulombic efficiency of the as-prepared device (Figure 9b). Meantime, an IR drop cannot be found in GCD curves of the single symmetric device at different current densities, suggesting that the MnO_2/GF composite system has low internal resistance, which is consistent with the results of the three-electrode construction. Based on the above discussion, we use a red light-emitting diode (LED) to detect the electrochemical energy storage of the MnO_2/GF||MnO_2/GF symmetric supercapacitor device. Since the rated voltage of the selected red LED was between 1.8 and 3.5 V, while the working voltage of the prepared single device was between −0.3 and 0.4 V, five single devices were therefore connected in series to ensure that the rated voltage of the five-series system matched that of the red LED. As shown in Figure 9c,d, the spread voltage of the CV and GCD curves of the five-series system is close to 3.5 V, and the red LED can be easily lighted up for about 10 min, as shown in Figure 9e,f.

It is well known that different test conditions will affect the performance of a device. In order to achieve the best performance of the prepared MnO_2/GF||MnO_2/GF symmetric device, we try to extend the operating voltage of the single device from 0.7 V (−0.3 to 0.4 V) to 1.6 V (−0.6 to 1.0 V), as shown in Figure 10a. It is found that the CV curves of a single device are almost the same shape at different operating

https://doi.org/10.1021/acsomega.2c06506
ACS Omega 2022, 7, 48320−48331

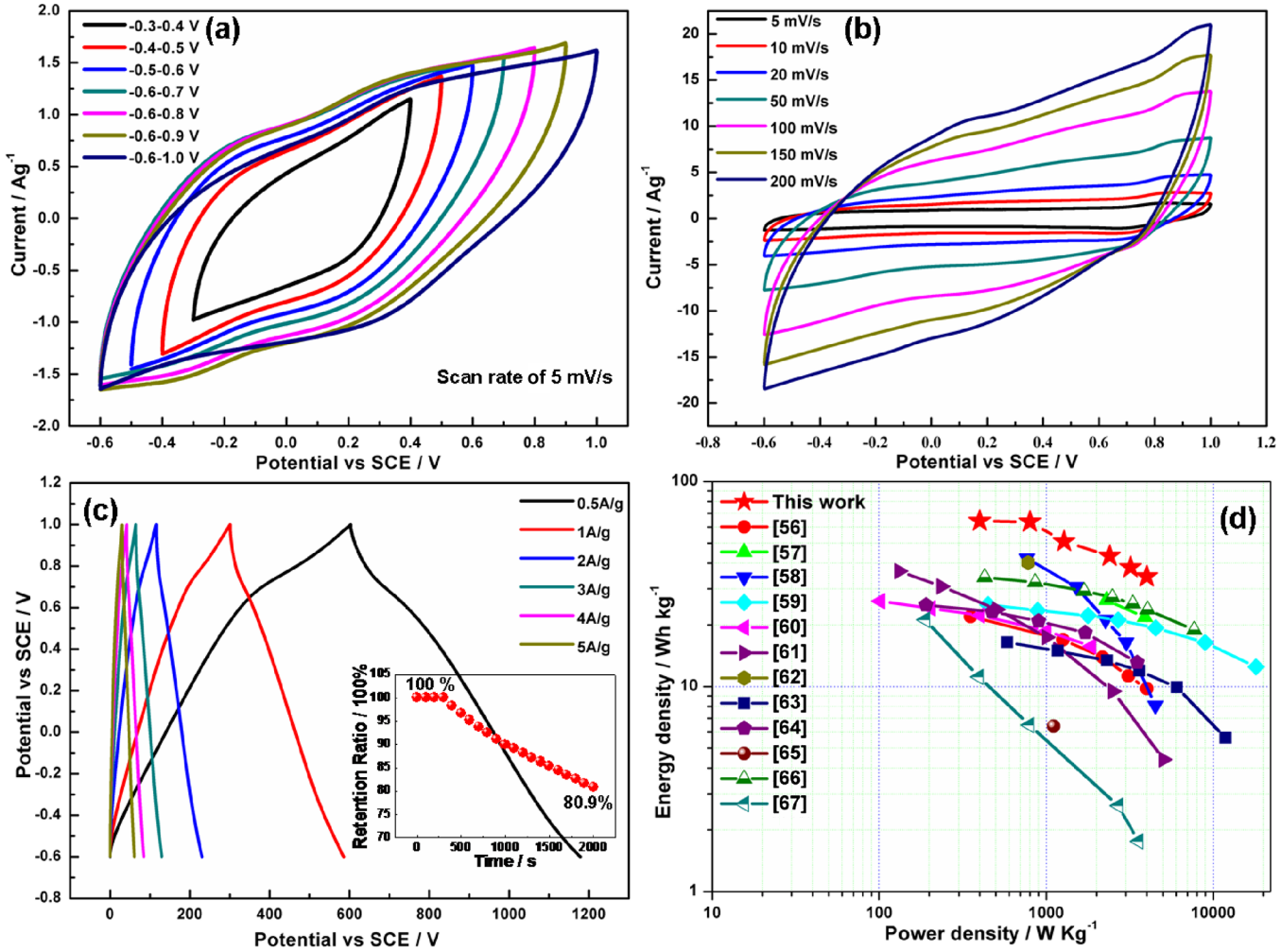

Figure 10. (a) CV curves of the single MnO_2/GF||MnO_2/GF device at different operating voltages ranging from 0.7 to 1.6 V. (b) CV curves of the single MnO_2/GF||MnO_2/GF symmetric device at different scan rates ranging from 5 to 200 mV/s (the applied voltage of a single device is 1.6 V). (c) GCD curves of the single MnO_2/GF||MnO_2/GF symmetric device at different current densities ranging from 0.5 to 5 A/g (the applied voltage of a single device is 1.6 V). The inset shows the long-term cycling stability of the MnO_2/GF||MnO_2/GF symmetric device. (d) Ragone plots of the as-assembled MnO_2/GF||MnO_2/GF device and previously reported literature.

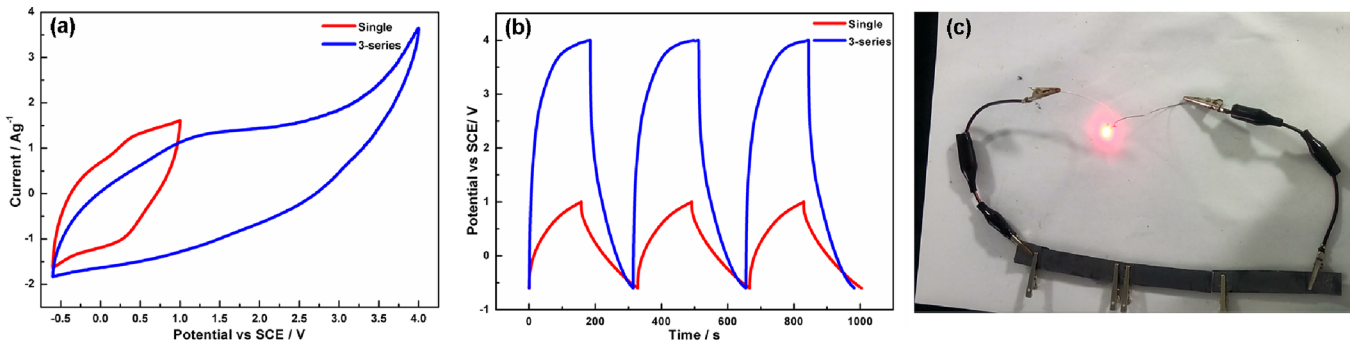

Figure 11. (a) CV curves of the single symmetric device and three-series system at a scan rate of 5 mV/s. (b) GCD curves of the single symmetric device and three-series system at a current density of 1 A/g. (c) Photograph of the red LED driven by the three-series tandem device.

voltages, indicating that the as-prepared symmetric device can stably work at 1.6 V when it is tested by two-electrode framework. Figure 10b shows that the CV curves of the single symmetric device also exhibit a quasi-rectangular shape at different scan rates, corresponding with the CV results of a single device under an operating voltage of 0.7 V (Figure 10a). The GCD curves of a single device under an operating voltage of 1.6 V can be seen in Figure 10c, and the SCs of a single device are calculated as 180.6, 179.0, 143.5, 121.9, 107.3, and 96.9 F/g at current densities of 0.5, 1, 2, 3, 4, and 5 A/g, respectively. The SC retention of the single MnO_2/GF||MnO_2/GF symmetric device can be maintained at about 80.9% after 2000 charge−discharge cycles at a current density of 10 A/g. It is lower than that of the single MnO_2/GF

https://doi.org/10.1021/acsomega.2c06506
ACS Omega 2022, 7, 48320−48331

electrode due to the stability of the device being worse than that of a single electrode in the same environment.

The energy density and power density can be obtained from our previously reported paper,[41] and the results can be found in Figure 10d. The maximum energy density (E) is 64.2 Wh/kg at a power density (P) of 400 W/kg; P can reach up to 4000 W/kg at an E of 34.4 Wh/kg. This value is superior to those of previously reported MnO_2-based systems, for example, rGO-mixed LaCe@MnO_2,[56] a-MnO_2@Ag@AAO,[57] MnO_2@N-PC,[58] MnO_2@rEGO,[59] defective mesoporous carbon/MnO_2,[60] CNT@MnO_2/EGP,[61] FeOOH@MnO_2,[62] activated carbon/MnO_2,[63] MnO_2@3D cross-linked carbon nanosheets,[64] carbon fabric@MnO_2//carbon fabric-MXene,[65] MnO_2-decorated hierarchical porous carbon,[66] and rGO/C/MnO_2,[67] as shown in Figure 10d. As shown in Figure 11a,b, the spread voltage of the CV and GCD curves of the three-series system is close to 4.8 V, and the red LED can be easily lighted up. Moreover, the brightness of the three-series device (4.8 V) is much higher than that of the five-series device (3.5 V), as shown in Figure 11c, showing that the applied voltage of a single device from 0.7 to 1.6 V can effectively increase the energy storage of the device.

4. CONCLUSION

In this work, MnO_2 nanosheets were successfully in situ prepared on a high-purity GF using a facile one-step hydrothermal method. The excellent electrical conductivity of graphite sheets and the structure of manganese dioxide nanosheets could be used as substrates for fast electron transfer and provide a good platform for anchoring pseudocapacitive active materials. The SC value of the single MnO_2/GF electrode was 882 F/g at 1.0 A/g, and its SC retention was about 90.1% after 5000 charge−discharge cycles at 10 A/g. The high performance is attributed to the deposition of thin-layer MnO_2 nanosheets with abundant interstitial spaces on the surface of the highly conductive GF, leading to more and more ions penetrating into the interior of the MnO_2 nanosheets to participate in the reaction to generate a high SC. Moreover, two sheets of MnO_2/GF electrodes and filter paper with a 1 M KOH/PVA gel electrolyte as a separator were stacked together to form an all-solid-state MnO_2/GF‖MnO_2/GF supercapacitor device. The electrochemical performance of a single device was measured at applied voltages of 0.7 and 1.6 V, and the single symmetric device displayed a high energy density of 64.2 Wh/kg at a power density of 400 W/kg with an applied voltage of 1.6 V. In addition, the red LED can be easily lighted up with the five-series tandem device (the applied voltage of a single device was 0.7 V) and three-series tandem device (the applied voltage of a single device was 1.6 V) as the power source. The results indicated that the MnO_2-nanosheet-modified GF composite is a promising material that can be applied in future high-performance supercapacitors.

AUTHOR INFORMATION

Corresponding Authors

Chenglong Hu − *Key Laboratory of Optoelectronic Chemical Materials and Devices, Ministry of Education, School of Optoelectronic Materials & Technology, Jianghan University, Wuhan 430056, P. R. China;* orcid.org/0000-0003-1554-269X; Email: ceshcl@jhun.edu.cn

Huabo Huang − *Hubei Key Laboratory of Plasma Chemistry and Advanced Materials, State Key Laboratory of Advanced Technology for Materials Synthesis and Processing, School of Materials Science and Engineering, Wuhan Institute of Technology, Wuhan 430205, P. R. China;* orcid.org/0000-0001-5545-5916; Email: hbhuang@wit.edu.cn

Authors

Yuanhang Gu − *Key Laboratory of Optoelectronic Chemical Materials and Devices, Ministry of Education, School of Optoelectronic Materials & Technology, Jianghan University, Wuhan 430056, P. R. China; Hubei Key Laboratory of Plasma Chemistry and Advanced Materials, State Key Laboratory of Advanced Technology for Materials Synthesis and Processing, School of Materials Science and Engineering, Wuhan Institute of Technology, Wuhan 430205, P. R. China*

Dong Xu − *Key Laboratory of Optoelectronic Chemical Materials and Devices, Ministry of Education, School of Optoelectronic Materials & Technology, Jianghan University, Wuhan 430056, P. R. China*

Shaoyun Chen − *Key Laboratory of Optoelectronic Chemical Materials and Devices, Ministry of Education, School of Optoelectronic Materials & Technology, Jianghan University, Wuhan 430056, P. R. China*

Feng You − *Hubei Key Laboratory of Plasma Chemistry and Advanced Materials, State Key Laboratory of Advanced Technology for Materials Synthesis and Processing, School of Materials Science and Engineering, Wuhan Institute of Technology, Wuhan 430205, P. R. China*

Jian Chen − *Instrumental Analysis and Research Center, Sun Yat-sen University, Guangzhou 510275, P. R. China;* orcid.org/0000-0001-5725-4368

Complete contact information is available at: https://pubs.acs.org/10.1021/acsomega.2c06506

Author Contributions

‖Y.G. and D.X. contributed equally to this work.

Notes

The authors declare no competing financial interest.

ACKNOWLEDGMENTS

The authors gratefully acknowledge the support of the National Natural Science Foundation of China (Grant No. 51973244), Natural Science Foundation of Hubei Province (Grant No. 2021CFB507), and Open Project of State Key Laboratory of Advanced Technology for Materials Synthesis and Processing (Wuhan University of Technology) (Grant No. 2022-KF-18).

REFERENCES

(1) Sharma, K.; Arora, A.; Tripathi, S. K. Review of supercapacitors: Materials and devices. *J. Energy Storage* **2019**, *21*, 801−825.

(2) Chatterjee, D. P.; Nandi, A. K. A review on the recent advances in hybrid supercapacitors. *J. Mater. Chem. A* **2021**, *9*, 15880−15918.

(3) Forouzandeh, P.; Kumaravel, V.; Pillai, S. C. Electrode materials for supercapacitors: a review of recent advances. *Catalysts* **2020**, *10*, 969.

(4) Liu, H.; Liu, X.; Wang, S.; Liu, H. K.; Li, L. Transition metal based battery-type electrodes in hybrid supercapacitors: A review. *Energy Storage Mater.* **2020**, *28*, 122−145.

(5) Delbari, S. A.; Ghadimi, L. S.; Hadi, R.; Farhoudian, S.; Nedaei, M.; Babapoor, A.; Namini, A. S.; Le, Q. V.; Shokouhimehr, M.; Asl, M. S.; Mohammadi, M. Transition metal oxide-based electrode materials for flexible supercapacitors: A review. *J. Alloys Compd.* **2021**, *857*, No. 158281.

(6) Wang, G.; Zhang, L.; Zhang, J. A review of electrode materials for electrochemical supercapacitors. *Chem. Soc. Rev.* **2012**, *41*, 797−828.
(7) Zhang, L. L.; Zhao, X. S. Carbon-based materials as supercapacitor electrodes. *Chem. Soc. Rev.* **2009**, *38*, 2520−2531.
(8) Liu, C. F.; Liu, Y. C.; Yi, T. Y.; Hu, C. C. Carbon materials for high-voltage supercapacitors. *Carbon* **2019**, *145*, 529−548.
(9) Liang, R. B.; Du, Y. Q.; Xiao, P.; Cheng, J. Y.; Yuan, S. J.; Chen, Y. L.; Yuan, J.; Chen, J. W. Transition metal oxide electrode materials for supercapacitors: a review of recent developments. *Nanomaterials* **2021**, *11*, 1248.
(10) Naskar, P.; Maiti, A.; Chakraborty, P.; Kundu, D.; Biswas, B.; Banerjee, A. Chemical supercapacitors: a review focusing on metallic compounds and conducting polymers. *J. Mater. Chem. A* **2021**, *9*, 1970−2017.
(11) Meng, Q.; Cai, K.; Chen, Y.; Chen, L. Research progress on conducting polymer based supercapacitor electrode materials. *Nano Energy* **2017**, *36*, 268−285.
(12) Li, L.; Meng, J.; Zhang, M.; Liu, T.; Zhang, C. Recent advances in conductive polymer hydrogel composites and nanocomposites for flexible electrochemical supercapacitors. *Chem. Commun.* **2021**, *58*, 185−207.
(13) Li, Y. M.; Han, X.; Yi, T. F.; He, Y. B.; Li, X. F. Review and prospect of $NiCo_2O_4$-based composite materials for supercapacitor electrodes. *J. Energy Chem.* **2019**, *31*, 54−78.
(14) Kate, R. S.; Khalate, S. A.; Deokate, R. J. Overview of nanostructured metal oxides and pure nickel oxide (NiO) electrodes for supercapacitors: A review. *J. Alloys Compd.* **2018**, *734*, 89−111.
(15) Wang, X. L.; Hu, A. Y.; Meng, C.; Wu, C.; Yang, S. B.; Hong, X. D. Recent advance in Co_3O_4 and Co_3O_4-containing electrode materials for high-performance supercapacitors. *Molecules* **2020**, *25*, 269.
(16) Jayakumar, A.; Antony, R. P.; Wang, R.; Lee, J. M. MOF-derived hollow cage $NixCo_3$-xO_4 and their synergy with graphene for outstanding supercapacitors. *Small* **2017**, *13*, 1603102.
(17) Yang, J.; Xiao, X.; Chen, P.; Zhu, K.; Cheng, K.; Ye, K.; Wang, G. L.; Cao, D. X.; Yan, J. Creating oxygen-vacancies in MoO_3-x nanobelts toward high volumetric energy-density asymmetric supercapacitors with long lifespan. *Nano Energy* **2019**, *58*, 455−465.
(18) Bhat, T. S.; Jadhav, S. A.; Beknalkar, S. A.; Patil, S. S.; Patil, P. S. MnO_2 core-shell type materials for high-performance supercapacitors: A short review. *Inorg. Chem. Commun.* **2022**, *141*, No. 109493.
(19) Zhang, W.; Shahnavaz, Z.; Yan, X.; Huang, X.; Wu, S.; Chen, H.; Pan, J.; Li, T.; Wang, J. One-step solvothermal synthesis of raspberry-like nico-mof for high-performance flexible supercapacitors for a wide operation temperature range. *Inorg. Chem.* **2022**, *61*, 15287−15301.
(20) Zhang, W.; Yuan, X.; Yan, X.; You, M.; Jiang, H.; Miao, J.; Li, Y.; Zhou, W.; Zhu, Y.; Cheng, X. Tripotassium citrate monohydrate derived carbon nanosheets as a competent assistant to manganese dioxide with remarkable performance in the supercapacitor. *Front. Chem. Sci. Eng.* **2022**, *16*, 420−432.
(21) Li, L.; Wen, J.; Zhang, X. Progress of two-dimensional Ti_3C_2Tx in supercapacitors. *ChemSusChem* **2020**, *13*, 1296−1329.
(22) Li, J. E.; Wang, Y. W.; Xu, W. N.; Wang, Y.; Zhang, B.; Luo, S.; Zhou, X. Y.; Zhang, C. L.; Gu, X.; Hu, C. G. Porous Fe_2O_3 nanospheres anchored on activated carbon cloth for high-performance symmetric supercapacitors. *Nano Energy* **2019**, *57*, 379−387.
(23) Bi, W.; Wang, J.; Jahrman, E. P.; Seidler, G. T.; Gao, G.; Wu, G.; Cao, G. Interface engineering V_2O_5 nanofibers for high-energy and durable supercapacitors. *Small* **2019**, *15*, 1901747.
(24) Asbani, B.; Buvat, G.; Freixas, J.; Huvé, M.; Troadec, D.; Roussel, P.; Brousse, T.; Lethien, C. Ultra-high areal capacitance and high rate capability RuO_2 thin film electrodes for 3D micro-supercapacitors. *Energy Storage Mater.* **2021**, *42*, 259−267.
(25) Huang, Y.; Li, Y.; Zhang, G. Y.; Liu, W.; Li, D.; Chen, R. S.; Zhen, F.; Ni, H. W. Simple synthesis of 1D, 2D and 3D WO_3 nanostructures on stainless steel substrate for high-performance supercapacitors. *J. Alloys Compd.* **2019**, *778*, 603−611.
(26) An, C. H.; Zhang, Y.; Guo, H. N.; Wang, Y. J. Metal oxide-based supercapacitors: progress and prospectives. *Nanoscale Adv.* **2019**, *1*, 4644−4658.
(27) Zhang, Q. Z.; Zhang, D.; Miao, Z. C.; Zhang, X. L.; Chou, S. L. Research progress in MnO_2−carbon based supercapacitor electrode materials. *Small* **2018**, *14*, 1702883.
(28) Majumdar, D. Review on current progress of MnO_2-based ternary nanocomposites for supercapacitor applications. *ChemElecTroChem* **2021**, *8*, 291−336.
(29) Li, Y.; Jiang, H.; Yan, X.; Zhang, W.; Zhang, M.; Zhu, W.; Pan, J.; Javed, M. S.; Cheng, W.; Guan, Y. Rationally designed Mn2O3/CuxO core-shell heterostructure generated on copper foam as binder-free electrode for flexible asymmetric supercapacitor. *Appl. Surf. Sci.* **2021**, *566*, No. 150715.
(30) Miao, J.; Zhou, C.; Yan, X.; Jiang, H.; You, M.; Zhu, Y.; Li, Y.; Zhou, W.; Cheng, X. Electrochemical performance of an asymmetric coin cell supercapacitor based on marshmallow-like MnO_2/carbon cloth in neutral and alkaline electrolytes. *Energy Fuels* **2021**, *35*, 2766−2774.
(31) Kour, S.; Tanwar, S.; Sharma, A. L. A review on challenges to remedies of MnO_2 based transition-metal oxide, hydroxide, and layered double hydroxide composites for supercapacitor applications. *Mater. Today Commun.* **2022**, *32*, No. 104033.
(32) Yu, Z.; Duong, B.; Abbitt, D.; Thomas, J. Highly ordered MnO_2 nanopillars for enhanced supercapacitor performance. *Adv. Mater.* **2013**, *25*, 3302−3306.
(33) Zhang, M.; Chen, Y.; Yang, D. Y.; Li, J. T. High performance MnO_2 supercapacitor material prepared by modified electrodeposition method with different electrodeposition voltages. *J. Energy Storage* **2020**, *29*, No. 101363.
(34) Wu, C.; Zhu, Y.; Ding, M.; Jia, C. K.; Zhang, K. L. Fabrication of plate-like MnO_2 with excellent cycle stability for supercapacitor electrodes. *Electrochim. Acta* **2018**, *291*, 249−255.
(35) Sun, P.; Yi, H.; Peng, T. Q.; Jing, Y. T.; Wang, R. J.; Wang, H. W.; Wang, X. F. Ultrathin MnO_2 nanoflakes deposited on carbon nanotube networks for symmetrical supercapacitors with enhanced performance. *J. Power Sources* **2017**, *34*, 27−35.
(36) Zhao, Y.; Hao, H. L.; Song, T. L.; Wang, X.; Li, C. W.; Li, W. Y. MnO_2-graphene based composites for supercapacitors: synthesis, performance and prospects. *J. Alloys Compd.* **2022**, *9141*, 65343.
(37) Yue, T.; Shen, B.; Gao, P. Carbon material/MnO_2 as conductive skeleton for supercapacitor electrode material: A review. *Renewable Sustainable Energy Rev.* **2022**, *158*, No. 112131.
(38) Jia, H. N.; Cai, Y. F.; Zheng, X. H.; Lin, J. H.; Liang, H. Y.; Qi, J. L.; Cao, J.; Feng, J. C.; Fei, W. D. Mesostructured carbon nanotube-on-MnO_2 nanosheet composite for high-performance supercapacitors. *ACS Appl. Mater. Interfaces* **2018**, *10*, 38963−38969.
(39) Saraf, M.; Natarajan, K.; Mobin, S. M. Robust nanocomposite of nitrogen-doped reduced graphene oxide and MnO_2 nanorods for high-performance supercapacitors and nonenzymatic peroxide sensors. *ACS Sustainable Chem. Eng.* **2018**, *6*, 10489−10504.
(40) Li, J. P.; Ren, Z. H.; Wang, S. G.; Ren, Y. Q.; Qiu, Y. J.; Yu, J. MnO_2 nanosheets grown on internal surface of macroporous carbon with enhanced electrochemical performance for supercapacitors. *ACS Sustainable Chem. Eng.* **2016**, *4*, 3641−3648.
(41) Liu, B.; Zhang, X. Y.; Tian, D.; Li, Q.; Zhong, M.; Chen, S. Y.; Hu, C. L.; Ji, H. B. In Situ Growth of Oriented Polyaniline Nanorod Arrays on the Graphite Flake for High-Performance Supercapacitors. *ACS Omega* **2020**, *5*, 32395−32402.
(42) Hu, C. L.; Zhang, X. Y.; Liu, B.; Chen, S. Y.; Liu, X. Q.; Liu, Y. M.; Liu, J. Y.; Chen, J. Orderly and highly dense polyaniline nanorod arrays fenced on carbon nanofibers for all-solid-state flexible electrochemical energy storage. *Electrochim. Acta* **2020**, *338*, No. 135846.
(43) Tian, D.; Cheng, H.; Li, Q.; Song, C.; Wu, D.; Zhao, X. Y.; Hu, S. Q.; Chen, S. Y.; Hu, C. L. The ordered polyaniline nanowires wrapped on the polypyrrole nanotubes as electrode materials for electrochemical energy storage. *Electrochim. Acta* **2021**, *398*, No. 139328.

https://doi.org/10.1021/acsomega.2c06506
ACS Omega 2022, 7, 48320−48331

(44) Chen, S. Y.; Liu, B.; Zhang, X. Y.; Chen, F.; Shi, H.; Hu, C. L.; Chen, J. Growth of polyaniline on TiO_2 tetragonal prism arrays as electrode materials for supercapacitor. *Electrochim. Acta* **2019**, *300*, 373−379.
(45) Chen, S. Y.; Cheng, H.; Tian, D.; Li, Q.; Zhong, M.; Chen, J.; Hu, C. L.; Ji, H. B. Controllable synthesis, core-shell nanostructures, and supercapacitor performance of highly uniform polypyrrole/polyaniline nanospheres. *ACS Appl. Energy Mater.* **2021**, *4*, 3701−3711.
(46) Peng, S.; Liu, B.; Zhang, X. Y.; Li, W. H.; Chen, S. Y.; Hu, C. L.; Liu, X. Q.; Liu, J. Y.; Chen, J. Large-Area Polyaniline Nanorod Growth on a Monolayer Polystyrene Nanosphere Array as an Electrode Material for Supercapacitors. *ACS Appl. Energ. Mater.* **2021**, *4*, 14766−14777.
(47) Zhu, J. Y.; Zhang, D. D.; Zhu, Z. C.; Wu, Q. S.; Li, J. F. Review and prospect of MnO_2-based composite materials for supercapacitor electrodes. *Ionics* **2021**, *27*, 3699−3714.
(48) Sun, G. L.; Li, X. J.; Qu, Y. D.; Wang, X. H.; Yan, H. H.; Zhang, Y. J. Preparation and characterization of graphite nanosheets from detonation technique. *Mater. Lett.* **2008**, *62*, 703−706.
(49) Li, Z. Q.; Lu, C. J.; Xia, Z. P.; Zhou, Y.; Luo, Z. X-ray diffraction patterns of graphite and turbostratic carbon. *Carbon* **2007**, *45*, 1686−1695.
(50) Khandare, L.; Terdale, S. Gold nanoparticles decorated MnO_2 nanowires for high performance supercapacitor. *Appl. Surf. Sci.* **2017**, *418*, 22−29.
(51) Blyth, R. I. R.; Buqa, H.; Netzer, F. P.; Ramsey, M. G.; Besenhard, J. O.; Golob, P.; Winter, M. XPS studies of graphite electrode materials for lithium ion batteries. *Appl. Surf. Sci.* **2000**, *167*, 99−106.
(52) Stranick, M. A. MnO_2 by XPS. *Surf. Sci. Spectra* **1999**, *6*, 31−38.
(53) Jia, H. N.; Cai, Y. F.; Lin, J. H.; Liang, H. Y.; Qi, J. L.; Cao, J.; Feng, J. C.; Fei, W. D. Heterostructural graphene quantum dot/MnO_2 nanosheets toward high-potential window electrodes for high-performance supercapacitors. *Adv. Sci.* **2018**, *5*, 1700887.
(54) Dang, W. H.; Dong, C. J.; Zhang, Z. F.; Chen, G.; Wang, Y. D.; Guan, H. T. Self-grown MnO_2 nanosheets on carbon fiber paper as high-performance supercapacitors electrodes. *Electrochim. Acta* **2016**, *217*, 16−23.
(55) He, S. J.; Hu, C. X.; Hou, H. Q.; Chen, W. Ultrathin MnO_2 nanosheets supported on cellulose based carbon papers for high-power supercapacitors. *J. Power Sources* **2014**, *246*, 754−761.
(56) Rajagopal, R.; Ryu, K. S. Synthesis of La and Ce mixed MnO_2 nanostructure/rGO composite for supercapacitor applications. *ChemElectroChem* **2018**, *5*, 2218−2227.
(57) Kumar, A.; Sanger, A.; Kumar, A.; Mishra, Y. K.; Chandra, R. Performance of high energy density symmetric supercapacitor based on sputtered MnO_2 nanorods. *ChemistrySelect* **2016**, *1*, 3885−3891.
(58) Vargheese, S.; Muthu, D.; Pattappan, D.; Kavya, K. V.; Kumar, R. R.; Haldorai, Y. Hierarchical flower-like MnO_2@ nitrogen-doped porous carbon composite for symmetric supercapacitor: Constructing a 9.0 V symmetric supercapacitor cell. *Electrochim. Acta* **2020**, *364*, No. 137291.
(59) Wang, H.; Fu, Q.; Pan, C. X. Green mass synthesis of graphene oxide and its MnO_2 composite for high performance supercapacitor. *Electrochim. Acta* **2019**, *312*, 11−21.
(60) Mohammadi, N.; Pourreza, K.; Adeh, N. B.; Omidvar, M. Defective mesoporous carbon/MnO_2 nanocomposite as an advanced electrode material for supercapacitor application. *J. Alloys Compd.* **2021**, *883*, No. 160874.
(61) Li, X. Q.; Zhu, Z. X.; Ma, G.; Ding, Y.; Wang, J. L.; Ye, Z. G.; Peng, X. Y.; Li, D. S. novel synthesis and characterization of flexible mno_2/cnt composites co-deposited on graphite paper as supercapacitor electrodes. *J. Electron. Mater.* **2022**, *51*, 2982−2994.
(62) Du, K.; Wei, G. J.; Zhao, F. Z.; An, C.; Wang, H.; Li, J. Q.; An, C. H. Urchin-like FeOOH hollow microspheres decorated with MnO_2 for enhanced supercapacitor performance. *Sci. China Mater.* **2018**, *61*, 48−56.
(63) Tagsin, P.; Suksangrat, P.; Klangtakai, P.; Srepusharawoot, P.; Ruttanapun, C.; Kumnorkaew, P.; Amornkitbamrung, V. Electrochemical mechanisms of activated carbon, α-MnO_2 and composited activated carbon-α-MnO_2 films in supercapacitor applications. *Appl. Surf. Sci.* **2021**, *570*, No. 151056.
(64) Li, Y. J.; Yu, N.; Yan, P.; Li, Y. G.; Zhou, X. M.; Chen, S. L.; Wang, G. L.; Tong, W.; Fan, Z. J. Fabrication of manganese dioxide nanoplates anchoring on biomass-derived cross-linked carbon nanosheets for high-performance asymmetric supercapacitors. *J. Power Sources* **2015**, *300*, 309−317.
(65) Wei, Y. D.; Zheng, M. M.; Luo, W. L.; Dai, B.; Ren, J. J.; Ma, M. L.; Li, T.; Ma, Y. All pseudocapacitive MXene-MnO_2 flexible asymmetric supercapacitor. *J. Energy Storage* **2022**, *45*, No. 103715.
(66) Xie, Y.; Yang, C.; Chen, P.; Yuan, D. W.; Guo, K. K. MnO_2-decorated hierarchical porous carbon composites for high-performance asymmetric supercapacitors. *J. Power Sources* **2019**, *425*, 1−9.
(67) Zhang, H.; Lin, L. Y.; Wu, B.; Hu, N. Vertical carbon skeleton introduced three-dimensional MnO_2 nanostructured composite electrodes for high-performance asymmetric supercapacitors. *J. Power Sources* **2020**, *476*, No. 228527.

https://doi.org/10.1021/acsomega.2c06506
ACS Omega 2022, 7, 48320−48331